How to cite: *Angew. Chem. Int. Ed.* **2023**, *62*, e202305564
doi.org/10.1002/anie.202305564

Phototheranostics

Nanostructure-Driven Indocyanine Green Dimerization Generates Ultra-Stable Phototheranostics Nanoparticles

Nahyun Kwon[+], Gabriel O. Jasinevicius[+], Giulia Kassab, Lili Ding, Jiachuan Bu, Letícia P. Martinelli, Vinicius G. Ferreira, Alexander Dhaliwal, Harley H. L. Chan, Yulin Mo, Vanderlei S. Bagnato, Cristina Kurachi, Juan Chen, Gang Zheng,* and Hilde H. Buzzá**

Abstract: Indocyanine green (ICG) is the only near-infrared (NIR) dye approved for clinical use. Despite its versatility in photonic applications and potential for photothermal therapy, its photobleaching hinders its application. Here we discovered a nanostructure of dimeric ICG (Nano-dICG) generated by using ICG to stabilize nanoemulsions, after which ICG enabled complete dimerization on the nanoemulsion shell, followed by J-aggregation of ICG-dimer, resulting in a narrow, red-shifted (780 nm→894 nm) and intense (≈2-fold) absorbance. Compared to ICG, Nano-dICG demonstrated superior photothermal conversion (2-fold higher), significantly reduced photodegradation (−9.6 % vs. −46.3 %), and undiminished photothermal effect (7 vs. 2 cycles) under repeated irradiations, in addition to excellent colloidal and structural stabilities. Following intravenous injection, Nano-dICG enabled real-time tracking of its delivery to mouse tumors within 24 h by photoacoustic imaging at NIR wavelength (890 nm) distinct from the endogenous signal to guide effective photothermal therapy. The unprecedented finding of nanostructure-driven ICG dimerization leads to an ultra-stable phototheranostic platform.

Introduction

Photothermal therapy (PTT) uses a photothermal agent to generate heat when irradiated with light to eliminate target cancer cells.[1] The characteristics of a promising photothermal agent include biocompatibility, light absorption in the near-infrared (NIR) range to improve the light delivery to thicker or deeper tissues,[2] adequate photostability and elevated photothermal conversion efficiency (PCE).[3] The only clinically approved NIR dye by the Food and Drug Administration is Indocyanine Green (ICG), an amphiphilic molecule that has been widely researched for its photonic properties including PTT.[4] Although ICG has excellent biocompatibility,[5] its application in PTT has been limited due to aggregation and degradation in aqueous solutions,[6] short half-life in vivo[7] and poor photostability.[8] Nanotechnology has been widely utilized for improving ICG's hydrolytic stability and in vivo delivery,[9] including polymer-based nanoparticles,[10] lipid-based nanoparticles,[11] nanodroplets,[12] albumin nanoparticles,[13] and silica nanoparticles[14] which leads to enhanced tumor delivery by passive or active targeting abilities of nanoparticles. Despite these efforts, the poor photostability of ICG remains a limitation. Herein, we discovered a single ICG stabilized nanoemulsion that enabled 100 % ICG dimerization and J-aggregation spontaneously on its shell to afford a nanostructure of dimeric ICG (Nano-dICG) that demonstrated superior PCE, photostability, and structure stability over

[*] Dr. N. Kwon,[+] Dr. G. Kassab, L. Ding, J. Bu, A. Dhaliwal, Dr. H. H. L. Chan, Y. Mo, Dr. J. Chen, Prof. Dr. G. Zheng
Princess Margaret Cancer Centre, University Health Network
101 College Street, PMCRT 5-354,
Toronto, ON, M5G1L7 (Canada)
E-mail: juan.chen@uhnresearch.ca
gang.zheng@uhnres.utoronto.ca

Prof. Dr. H. H. Buzzá
Institute of Physics, Pontificia Universidad Católica de Chile
7820436, Santiago (Chile)
E-mail: hilde.buzza@uc.cl

A. Dhaliwal, Prof. Dr. G. Zheng
Department of Medical Biophysics, University of Toronto
Toronto, ON (Canada)

G. O. Jasinevicius,[+] Dr. G. Kassab, L. P. Martinelli, Dr. V. S. Bagnato, Prof. Dr. C. Kurachi, Prof. Dr. H. H. Buzzá
Sao Carlos Institute of Physics, University of Sao Paulo
Sao Carlos (Brazil)

Dr. V. G. Ferreira
Sao Carlos Institute of Chemistry, University of Sao Paulo
Sao Carlos (Brazil)

Y. Mo, Prof. Dr. G. Zheng
Institute of Medical Science, University of Toronto
Toronto, ON, Canada

Dr. V. S. Bagnato
Department of Biomedical Engineering, Texas A&M University
College Station (USA)

[+] These authors contributed equally to this work.

ICG, as well as spectral-distinct strong photoacoustic contrast, giving an ultra-stable phototheranostic platform (Scheme 1).

Results and Discussion

Synthesis and Characterization

A nanoemulsion was first produced by simply hydrating a film of ICG monomer and glyceryl trioctanoate oil mixture under sonication (see the method in the Supporting Information). Upon storage in an aqueous solution at 4 °C, ICG oxidative dimerization occurred on the core-shell nanostructure, leading to 100 % ICG dimerization at the nanoemulsion interface at day 16 post formulation, identified by UPLC-MS analysis. At 750 nm absorption channel, Nano-dICG showed a unique peak at retention time (RT) of 3.2 minutes with identified dimeric ICG (dICG) mass of 1503.44 [ESI$^+$[M]$^+$] (Figure 1a), distinguishing from the ICG monomer peak at RT of 3.4 minutes with a detected monomeric mass of 752.50 [ESI$^+$[M]$^+$] (Figure 1b). The

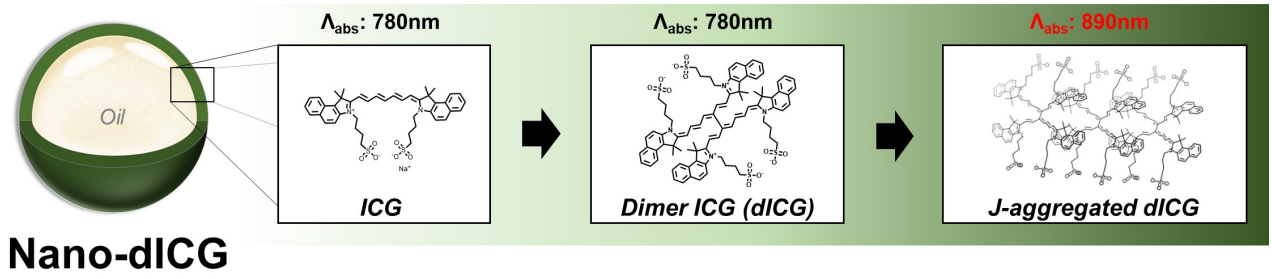

Scheme 1. This schematic represents the spontaneous induction of ICG dimerization and J-aggregation when preparing Nano-dICG using monomeric ICG.

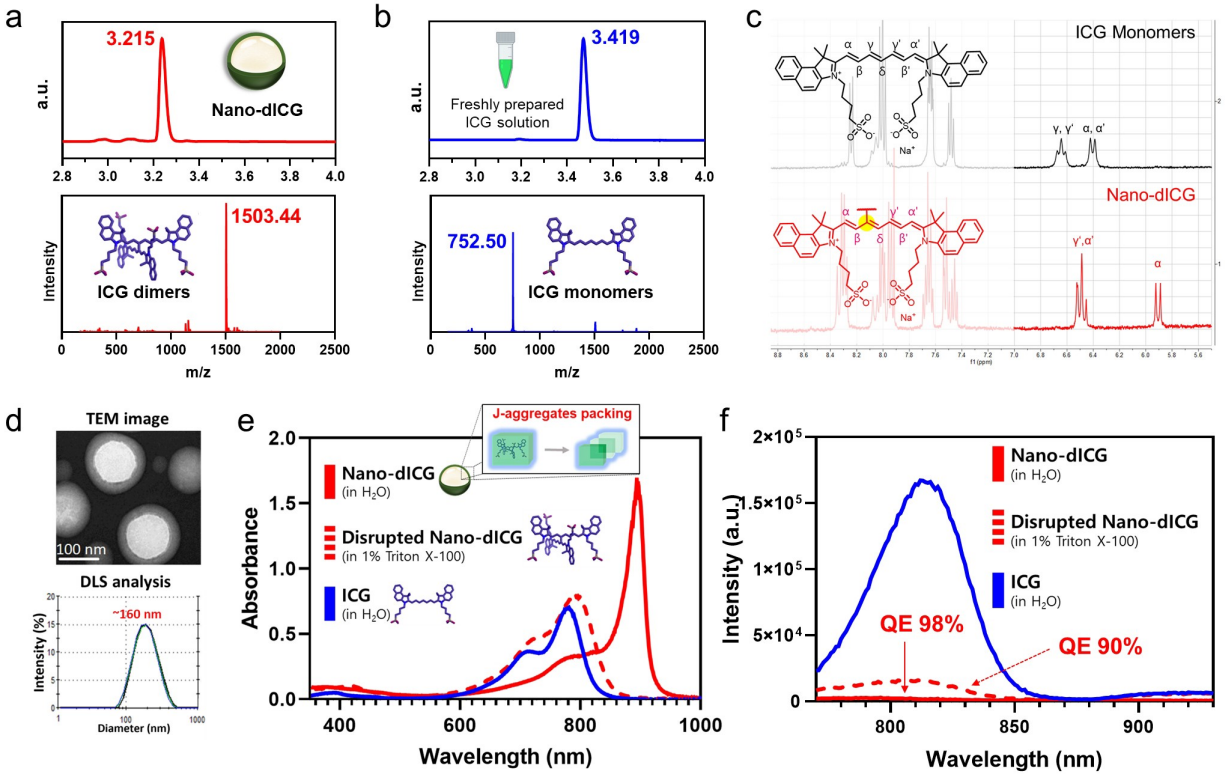

Figure 1. UPLC profiles and corresponding peaks' mass spectra a) of a Nano-dICG solution and b) of a fresh ICG solution. c) ^{1}H NMR analysis of ICG and dyes extracted from Nano-dICG. d) TEM microscopy image and DLS measured hydrodynamic diameter distribution of Nano-dICG. e) Absorbance spectra of Nano-dICG, ICG and disrupted Nano-dICG. f) Fluorescence generation of intact and disrupted Nano-dICG compared with ICG at normalized ICG concentration of 78 ng mL^{-1}.

corresponding UV/Vis absorption spectra of dICG (RT = 3.2 minutes) and ICG (RT = 3.4 minutes) acquired by a photodiode array detector of UPLC were similar (Figures S1a and S1b). Notably, the characters of the peak at RT 3.2 minutes belong to the dissociated dICG molecule as the nanostructure of Nano-dICG is disassembled during the reverse phase UPLC separation. The UPLC profile of co-injection of Nano-dICG and ICG monomer further confirmed unmixed dICG and ICG peaks at RT of 3.2 minutes and 3.4 minutes, respectively, with corresponding mass of 1503.62 [ESI$^+$[M]$^+$] and 752.59[ESI$^+$[M]$^+$] (Figure S1c). The ICG counterpart extracted from Nano-dICG was further subjected to nuclear magnetic resonance (NMR) spectroscopy analysis (Figure S2–S4). Compared to the ICG monomer, a distinct shift was observed in the hydrogen peak located at the gamma position of the alkyne chain in the ^{1}H NMR analysis of ICG counterpart extracted from Nano-dICG. (Figure 1c). This peak shift confirms the formation of dimer with a bond formed at the gamma position, which is consistent with the previously reported ^{1}H NMR of dICG.[15] Although it is known that highly concentrated ICG forms H-aggregates that favor the oxidative dimerization pathway,[16] a complete ICG dimerization was first reported here, permitting a pure dICG-formed nanoemulsion. The assessment of the mature Nano-dICG with complete dimerization was conducted by Transmission Electronic Microscope (TEM) and Dynamic Light Scattering (DLS) measurements, which revealed a monodispersed spherical shell-core structure of Nano-dICG with an average hydrodynamic diameter of approximately 160 nm (Figure 1d and S5) and zeta potential of approximately −50 mV (Table S1).

The optical properties of the Nano-dICG were first characterized by UV/Vis absorption spectrum measurement in an aqueous solution. The results showed a narrow, red-shifted peak (from 780 nm to 894 nm) with significantly increased absorbance compared to ICG (Figure 1e), which suggests the presence of J-aggregates.[17] Therefore, the high density of pure dICG alignment on the Nano-dICG shell facilitated their ordered arrangement, leading to the formation of J-aggregates. When Nano-dICG was disassembled in methanol or detergent-containing solution (1 vol% of Triton X-100), the J-aggregate related absorption disappeared, and the well-dispersed dICG exhibited a similar absorbance spectrum as monomeric ICG (Figure 1e). The extinction coefficient of Nano-dICG and ICG were determined in both H_2O and methanol based on ICG concentration (Figure S6). Nano-dICG showed unique high light absorption ($\varepsilon_{\lambda 890\,nm} = 411\,800\ cm^{-1}M^{-1}$) in aqueous solution, which is twice as high as ICG ($\varepsilon_{\lambda 780\,nm} = 181\,400\ cm^{-1}M^{-1}$). Under fluorescence measurement, Nano-dICG showed more than 98% fluorescence quenching compared to free ICG (Figure 1f). Interestingly, even when the disrupted Nano-dICG showed the absorption peak shifting back to 780 nm, its fluorescence generation remained more than 90% quenched, which indicates that the stable, highly quenched fluorescence in Nano-dICG is not only contributed by its nanostructure and J-aggregation but mainly attributed to dimeric ICG.

Kinetic Progression of Dimerization and J-aggregation of Nano-dICG

It is observed that the dimerization and J-aggregation of Nano-dICG do not occur immediately after the nanoparticle formulation. We then tracked the conversion progression over time by determining ICG fragments using UPLC and absorption red-shift with UV/Vis spectrum measurement. UPLC analysis revealed that ICG units in a freshly prepared formulation were present in monomer form and gradually turned into dICG over time during 4 °C storage. The conversion was completed at day 16 post-preparation (Figure 2a). The corresponding absorbance measurement (Figure 2b) also found an initial monomer ICG-peak at 780 nm for the freshly prepared Nano-dICG, followed by a gradual decrease in 780 nm absorption while an increase in J-shift peak at 890 nm over time, and finally reaching complete J-shift absorption at day 18 post-preparation. This indicates that dimer formation and J-aggregation occur almost simultaneously. In addition, the ICG fluorescence in freshly prepared samples was quenched by more than 70% due to the high density packing of monomeric ICG in the nanostructure. The quenched fluorescence could be completely

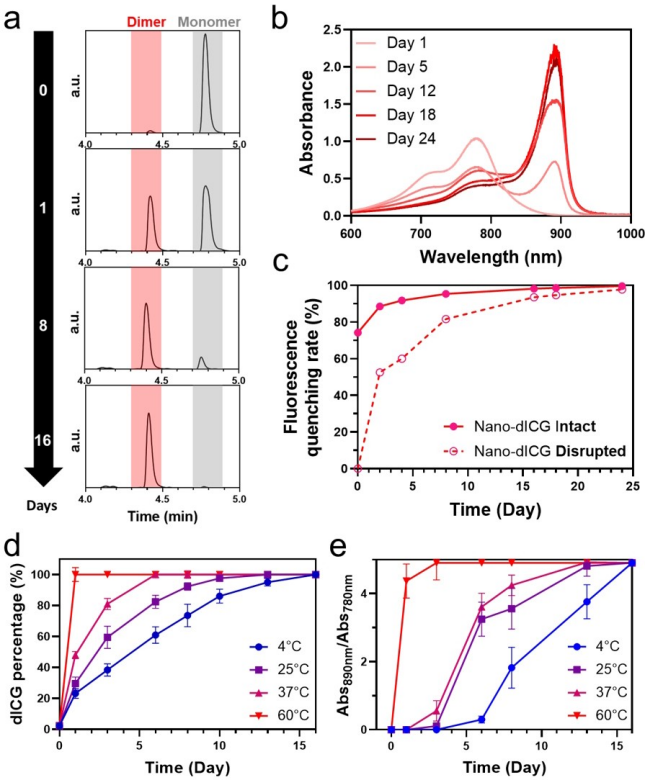

Figure 2. Dimerization and J-aggregation progression of Nano-dICG at 4 °C storage after nanoparticles preparation; a) UPLC profile revealed ICG gradual dimerization with time. b) The absorption spectra shift associated to J-aggregation was increased over time. c) Fluorescence quenching rate of Nano-dICG increased at either nanostructure intact or disrupted form. d) The proportion of dICG under UPLC analysis were traced over time for Nano-dICG when storage at different temperatures. e) The absorption shift rate ($A_{890\,nm}/A_{780\,nm}$) were traced over time. Data are expressed as the mean ± SD, $n = 3$ per group.

restored when the nanoparticles were disrupted in detergent-containing condition (Figure 2c). With the time increasing after Nano-dICG preparation, the fluorescence quenching rate continually increased in both intact and disrupted forms, corresponding to the proportionate increase of dimer and J-aggregate. The maximum fluorescence quenching rate was reached for both Nano-dICG intact (98 % fluorescence quenching) and disrupted phases (90 % fluorescence quenching) at day 18 after formulation. All the results together support the kinetic progress of ICG dimerization and J-aggregation in Nano-dICG at 4 °C storage. To investigate whether an increase in temperature could accelerate the progress, we kept the freshly prepared Nano-dICG aliquots at room temperature, 37 °C and 60 °C, respectively, to examine the dimerization kinetics and compared them with that at 4 °C storage. The dimerization conversion was tracked by dICG proportion using UPLC analysis (Figure 2d), and J-aggregation was monitored by the absorption signal ratio of $A_{890\,nm/780\,nm}$ (Figure 2e). The result revealed that the dimerization and J-aggregation of Nano-dICG at the highest temperature of 60 °C was completed in one day with the fastest rate, indicating that the dimerization and J-aggregation process is a thermodynamic process. Nano-dICG also enabled carrying an efficient amount of oxacillin (OX, 5.3 wt. %) or curcumin (CU, 2.3 wt. %) into its inner oil core (Figure S7) without changing its morphology or disrupting the process of dimerization and J-aggregation, thus demonstrating its function as a viable nanoparticle platform for additional drug delivery.

Nano-dICG Demonstrated Super Colloidal and Optical Stability

The poor stability of ICG under in vivo conditions is a major limitation that hinders ICG phototherapeutic application. Therefore, we investigated the stability of Nano-dICG under different solution conditions by varying pH, temperature and in a mimetic biological environment. We demonstrated that mature Nano-dICG (with complete dimerization) was colloidally and optically stable over a wide range of pH (pH 3–9) and temperature (0–60 °C), as evidenced by minimal changes in Nano-dICG size, absorbance shift, and fluorescence quenching efficiency (Figure 3a and b). Although the absorption ratio of 890 nm/780 nm partially decreased with increasing temperature, the J-shift peak of 890 nm was still the dominant peak ($A_{890nm}/A_{780nm} > 3$) at 60 °C. For in vivo application, various proteins in the blood stream could interact with ICG components to affect the stability of Nano-dICG. Therefore, we assessed its stability in a serum-mimetic condition using an aqueous solution containing 50 % fetal bovine serum (FBS). As shown in Figure 3c, the observed size increase of Nano-dICG over time was expected due to its bonding with the protein, while negligible changes were observed in its absorption shift and fluorescence quenching rate, indicating that the Nano-dICG remained intact and stable. Therefore, the unique photophysical properties of Nano-dICG could remain stable in complex in vivo environments.

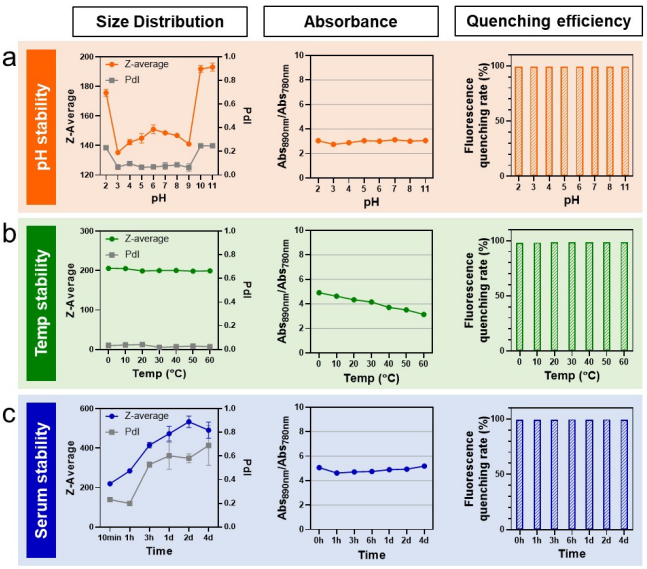

Figure 3. Nano-dICG demonstrated super colloidal and optical stability; The stability was evaluated by measuring changes in size and distribution, absorbance peak shift, and fluorescence quenching efficiency at a) varying pH, b) temperature and in a c) solution containing 50 % fetal bovine serum (FBS) for 4 days. Size distribution data are expressed as the mean ± SD, $n = 3$ per group.

To confirm that this distinctive phenomenon (100 % dimerization and J-aggregation) is a unique finding in Nano-dICG, we prepared a common ICG-incorporated nanoparticle, ICG liposome (ICGLP), and examined its structural and photophysical properties after storage at 4 °C for a month. The size distribution and morphology are shown in Figure S8a and S8b. Absorption measurements revealed no red-shift of absorption in ICGLP; instead, a slight blue-shift and decrease of absorbance were found, suggesting that the ICG in ICGLP might exist in H-aggregate form[18] (Figure S8c). Although intact ICGLP showed 59 % fluorescence quenching compared to free ICG, the quenched fluorescence could be 100 % restored when the nanostructure was disrupted (Figure S8d). In contrast, the Nano-dICG at nanostructure disruption still retained > 90 % fluorescence quenching (Figure 1f). UPLC-MS analysis further confirmed that the ICG component in ICGLP remained in monomeric form (Figure S9). Therefore, the phenomenon of complete ICG dimerization and J-aggregation is a unique finding in Nano-dICG.

Nano-dICG Demonstrated Superior Photothermal Conversion Efficiency and Photostability

Nano-dICG in both its nanostructure intact and disrupted forms showed over 10-fold reduction in fluorescence emission compared to ICG (Figure 1f), indicating that Nano-dICG in both forms absorbed significant NIR light while did not efficiently dissipate the absorbed energy via radiative decay.[11] Nano-dICG's light interaction was then characterized for its PCE by subjecting samples to light

irradiation (λ_{810nm}) in aqueous solution for 10 minutes at 3.9 $\mu g\,mL^{-1}$ to measure the samples' temperature changes. Nano-dICG gave a maximum temperature increase of 20.9 °C versus 10.5 °C by ICG (Figure 4a). The calculated PCE of Nano-dICG was 42.1 %, significantly higher than that of ICG (20.8 %). The PCE was also assessed for samples in detergent-containing solution, where the Nano-dICG and ICG were both well dispersed. Upon light irradiation for 5 minutes, the temperature increase reached up to 26.9 °C for the disrupted Nano-dICG and 13.6 °C for ICG (Figure S10), giving a PCE of 48 % and 19.5 %, respectively (Table S2). Even though the loss of radiative decay of dICG has been described beforehand,[22] this study provided a first-time demonstration of the improvement of PCE by dICG regardless of in nanostructure intact or disrupted form, which indicated that dimerization of ICG led to a favored thermal deactivation pathway.[19] In addition, the photostability measurement under continuous light irradiation (λ_{810nm}, 1 $W\,cm^{-2}$, 10 minutes, 156 $\mu g\,mL^{-1}$) revealed that Nano-dICG in either its intact or disrupted form performed significantly less absorption reduction than ICG (Figure 4b and S11). As summarized in Table S3, Nano-dICG in either intact or disrupted form exhibited robust photostability superior to ICG, with photodegradation rate reduced by 4.4-fold and 2.8-fold, respectively. Therefore, the complete dimeric ICG nanoemulsion provided a perfect platform to investigate the potential applications of this dICG organic molecule as a photothermal agent.

A deep evaluation of the photothermal efficacy of Nano-dICG was performed by varying the agent concentrations and light irradiance. It is unsurprising that ICG monomer enabled photothermal effect at a high concentration (e.g.,156 $\mu g\,mL^{-1}$), giving a temperature increase >40 °C similar to that caused by Nano-dICG in either intact or disrupted form (Figure S12a). However, within a low concentration range of 3.9 $\mu g\,mL^{-1}$ to 39 $\mu g\,mL^{-1}$, upon a light dose delivery of 600 $J\,cm^{-2}$, Nano-dICG enabled a maximum temperature greater than ICG under all experimental conditions (Figure S12b). At each condition case, Nano-dICG also enabled a sustained photothermal response with the sample's temperature continuously remained increased during 10 minutes of irradiation, whereas ICG caused the sample's temperature to increase initially, reach a maximum within 5 minutes and decrease gradually afterward, indicating remarkable photobleaching occurrence in ICG samples (Figure S12c and S12d). The greatest difference in the photothermal response between Nano-dICG and ICG was found at 15.6 $\mu g\,mL^{-1}$, where Nano-dICG enabled variation of temperature about 38.3 °C exceeding ICG's about 16.3 °C. The photothermal effect was next evaluated at this concentration (15.6 $\mu g\,mL^{-1}$) by varying light irradiance fluence (Figure S12e). At a low fluence rate of 0.3 W/cm^2 (90 $J\,cm^{-2}$), Nano-dICG generated a slight photothermal effect with a temperature increase of 12.5 °C, similar to ICG (11.5 °C). With increasing light irradiance, Nano-dICG demonstrated enhanced photothermal effect over ICG, resulting in temperature increases of 22.1 °C by 0.6 $W\,cm^{-2}$ (180 $J\,cm^{-2}$) and 29.6 °C by 0.9 $W\,cm^{-2}$ (270 $J\,cm^{-2}$), outperforming ICG by 6 °C and 11 °C, respectively. These data demonstrated more intense photothermal effect caused by Nano-dICG in response to higher light dose irradiance. Enhanced photostability of Nano-dICG over ICG was also confirmed with much slower absorption decay. As shown in Figure S12f, ICG at concentration of 15.6 $\mu g\,mL^{-1}$ showed quick absorption decay in corresponding to increase of light dose, while Nano-dICG showed significantly enhanced photostability under all the applied irradiances.

The influence of photobleaching on photothermal response was further characterized by "On/Off" irradiation cycles (Figure 4c). Although both ICG and Nano-dICG, at 39 $\mu g\,mL^{-1}$, enabled a temperature increase up to roughly 55 °C in the first cycle, ICG gradually showed a decreased photothermal effect throughout the cycles. The temperature reached only 36 °C on the 4th cycle and 32 °C on the 7th. Meanwhile, Nano-dICG enabled a more sustained temperature increase, reaching up to 59 °C on the 3rd cycle and 52 °C on the 7th cycle with 20 °C superior to ICG. The On/Off cycle tests were repeated for the disrupted Nano-dICG and ICG in a detergent-containing solution (both dICG and ICG are well-dispersed). Both samples demonstrated similar photothermal behavior at the first two cycles, enabling a temperature increase up to 59 °C. However, ICG monomer progressively diminished its photothermal effect, reaching only 39 °C on the 7th cycle, while the disrupted Nano-dICG (dICG) showed a consistent temperature increase of above 58 °C at each subsequent cycle. The excellent molecular stability of dICG compared to ICG when exposed to light was further validated by UPLC analysis of the samples after irradiation (Figure 4d and Figure S13). The data revealed that Nano-dICG maintained molecular and color stability during 7 cycles of irradiation, while ICG showed rapid diminishment of the molecular peak within 3 cycles, consistent with its color photobleaching. Therefore, the poor photostability of ICG results in a decreased number of activated molecules per cycle, meanwhile the dICG permits a more sustained number of activated molecules, thus providing a more robust photothermal effect in both Nano-dICG intact and disrupted form, which was supported by a mathematical model in the Supporting Information.

Nano-dICG Permitted Enhanced Photothermal Effect

The photothermal effect was next assessed in tissue-mimicking albumin phantoms that could simulate light scattering and absorption properties of biological tissues.[20] Phantoms were prepared by an overnight polymerization of a solution containing Nano-dICG, disrupted Nano-dICG or ICG (156 $\mu g\,mL^{-1}$). The phantoms were irradiated with a NIR laser (λ_{810nm}; 1 $W\,cm^{-2}$; 10 minutes) and the temperature increases were measured by a thermocouple allied with thermographic images (Figure 4e and f). Unlike ICG that caused an effective photothermal effect in aqueous solution at this concentration ($\Delta T > 40$ °C, Figure S12a), it gave only a 16 °C temperature increase in tissue-mimicking phantoms by thermocouple measurement. In contrast, both intact and disrupted Nano-dICG demonstrated significant photother-

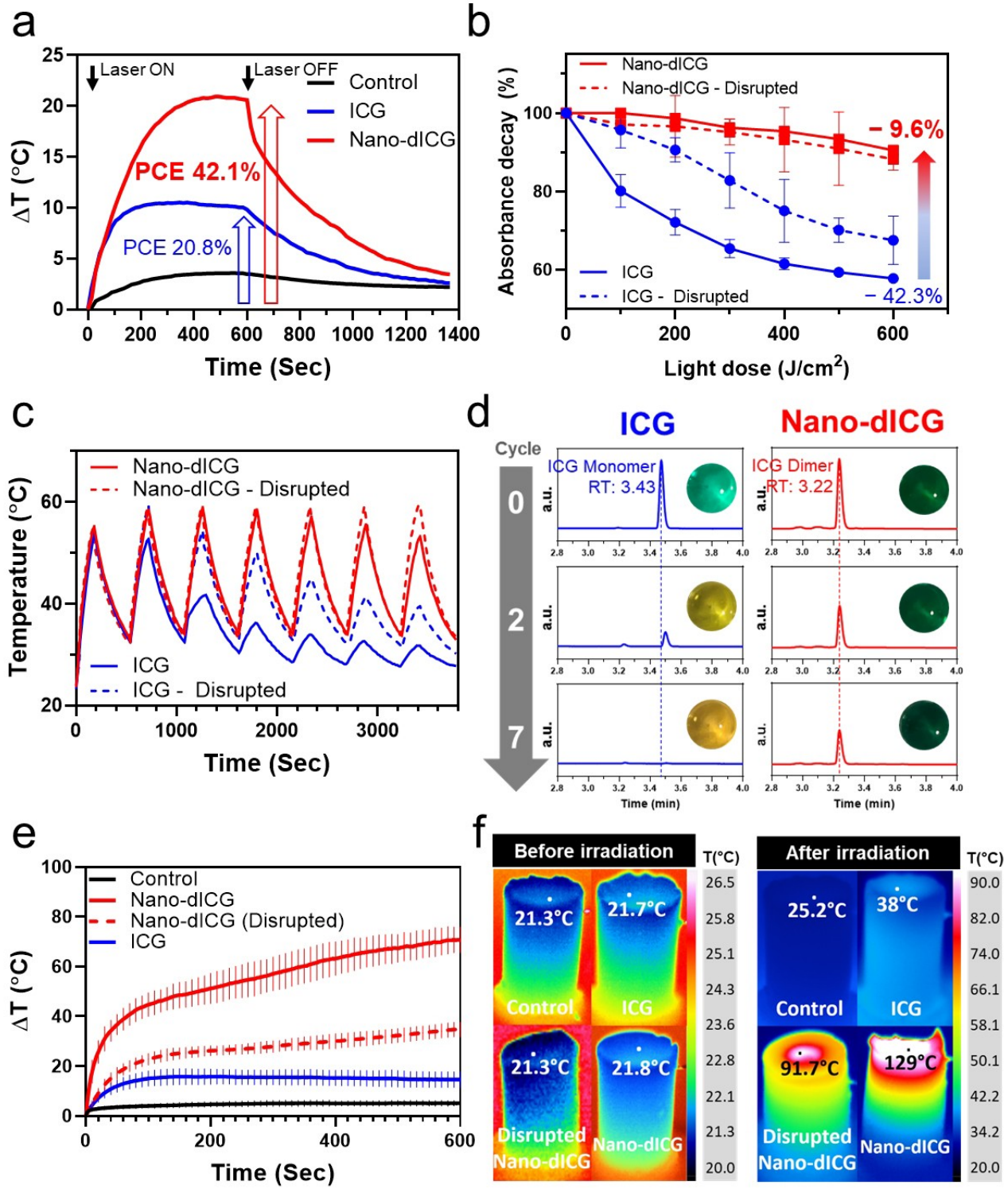

Figure 4. The photothermal effect of Nano-dICG and ICG; a) Calculated PCE of Nano-dICG and ICG at 3.9 μg mL^{-1} and b) absorbance decay curves of ICG and Nano-dICG at 156 μg mL^{-1} in different solvents after different dose of light treatment ($\lambda_{810nm,}$ data expressed in the mean value ± SD). c) Thermal response of Nano-dICG and ICG during 7 cycles of "On/Off" irradiation (1 W cm^{-2}, 9 minutes per cycle) at 39 μg mL^{-1} in different solvents. d) UPLC profile of Nano-dICG and ICG solution at before and after 2 and 7 cycles of "On/Off" irradiation ($\lambda_{825\,nm}$, 0.65 W cm^{-2}, 5 minutes per cycle) at 39 μg mL^{-1} in water (inset picture showed color change of solution after irradiation). Photothermal effect in tissue-mimicking albumin phantoms containing samples at concentration of 156 μg mL^{-1} by laser irradiation (λ_{810nm}, 1 W cm^{-2}, 10 minutes). e) Real-time tracking temperature changes by a thermocouple (Data expressed in the mean value ± SD) and f) thermographic images measured temperature before and after 10 minutes irradiation.

mal effects in tissue-mimicking phantoms with temperature increased by 70 °C and 40 °C, respectively. The remarkable photothermal efficacy of dICG was reaffirmed by thermographic images that revealed maximumly reached temperature of 129 °C by Nano-dICG, 91.7 °C by disrupted Nano-dICG, while 38 °C by ICG. Therefore, compared to ICG monomeric counterpart, dICG demonstrated greater photothermal effect in tissue-mimetic phantoms and a nanostructure of dICG enabled further enhanced efficiency of converting light into heat.

Nano-dICG Enabled Spectral-Distinct Photoacoustic Imaging

Great PCE of Nano-dICG suggests its potential utility in photoacoustic (PA) imaging.[21] We then evaluated its PA imaging ability on a thin tubing phantom. The tubes filled with ICG, intact/disrupted Nano-dICG, or intact/disrupted ICGLP (ICG nanoparticle control), were subjected to PA spectra scan using a Vevo LAZR 2100 (VisualSonics). The results showed that Nano-dICG produced a strong PA signal in the NIR region of 890 nm, which is 17 times higher than that of free ICG at the same concentration (Figure 5a and b). This strong PA signal is clearly separated from the endogenous hemoglobin signal,[22] thus favoring in vivo PA imaging and quantification. It is also important to note that the disrupted Nano-dICG exhibited a strong spectral-distinct PA signal at 780 nm, 2.5-fold higher than that of free ICG, which was consistent with the PCE enhancement (2.5-fold) by dimeric ICG (Table S2). In contrast, ICGLP showed a strong wide PA signal ranging from 700 to 820 nm due to its nanostructure and possible H-aggregate of ICG, while the signal was eliminated after nanoparticle dissociation.

We next investigated the potential use of PA signal for concentration determination of intact (PA signal at 890 nm) and disrupted Nano-dICGs (PA value at 780 nm). The results demonstrated a positive linear correlation between their concentration and corresponding PA signals, within the concentration range of 7.8–195 $\mu g\,mL^{-1}$ (Figure 5c and d). After confirming no cytotoxicity of Nano-dICG to 4T1 breast cancer cells in the concentration range of 2.0–126.4 $\mu g\,mL^{-1}$ (Figure S14), we then preformed PA imaging and PA spectral scans on the 4T1 cells after incubating with Nano-dICG for different periods. As shown in Figure S15, the PA signal at 890 nm increased continually with increasing incubation time and reached a plateau at 10 h of incubation, remaining at a high level up to 24 h. In addition, the PA signal at 780 nm appeared after 6 h and increased remarkably, indicating that Nano-dICG partially dissociated inside the cell over time. However, the PA signal at 890 nm remained in majority at 24 h of incubation. These data suggests that Nano-dICG enters cells very efficiently and the majority remains intact in cells for at least 24 h. This finding also provides feasibility for using ratiometric PA imaging (spectral-distinct PA signal ratio of 890 nm/780 nm) to track Nano-dICG delivery and its dissociation progress.

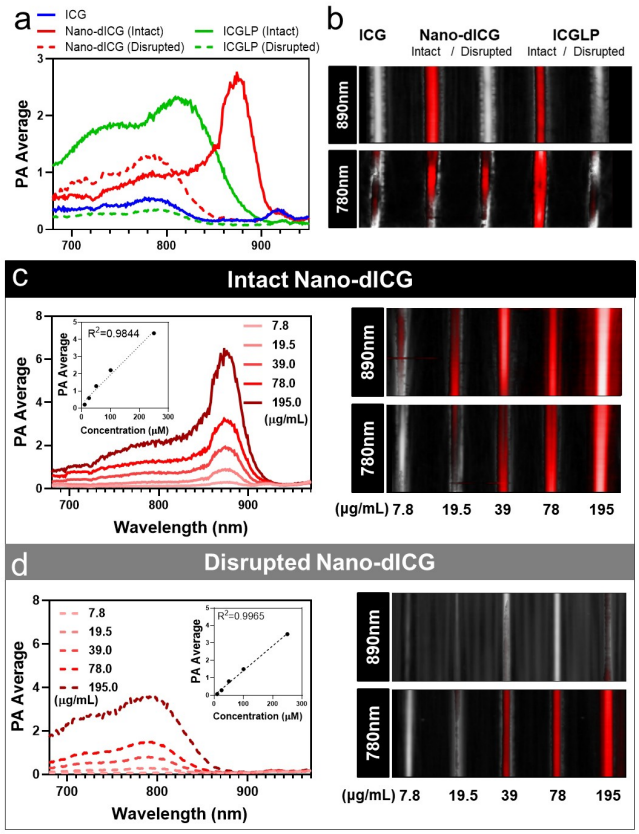

Figure 5. a) PA spectra and b) PA images of thin tubing phantoms containing ICG, intact Nano-dICG, disrupted Nano-dICG, intact ICGLP and disrupted ICGLP at 890 nm and 780 nm. The ICG concentration of all samples was 38.8 $\mu g\,mL^{-1}$, and 2% Triton X-100 in ddH_2O solution was used to disrupt the nanoparticles. PA spectra and images of thin tube phantoms containing c) different concentrations of intact Nano-dICG and d) disrupted Nano-dICG at 890 nm and 780 nm.

In Vivo PA Imaging of Tumor in An Orthotopic Breast Cancer Mouse Model

With its unique photonic properties and stellar colloidal and serum stabilities, Nano-dICG was next investigated for in vivo PA imaging on 4T1 orthotopic breast cancer mouse model.[23] ICGLP was used as a general ICG-loaded nanoparticle control. The in vivo PA spectrum scan was conducted on the tumor site of mice at pre-injection, 1 h, 6 h, and 24 h post intravenous injection of Nano-dICG or ICGLP. A strong and distinguishable PA signal at 890 nm in the tumors of the Nano-dICG group was detected 1 h post injection (Figure 6a, Figure S16 ($n=3$)). The PA signal at 890 nm gradually decreased over time but remained highly available and dominant at 24 h post injection, indicating that Nano-dICG stably maintained its integrity in tumor and its PA signal allowed for real-time tracking of its accumulation in tumors to guide treatment. In contrast, no detectable PA signal was found in tumors of ICGLP group across all time points (Figure 6b, Figure S17 ($n=3$)), despite validating significant tumor accumulation of ICGLP by the strong tumor fluorescence signal upon whole-body fluorescence

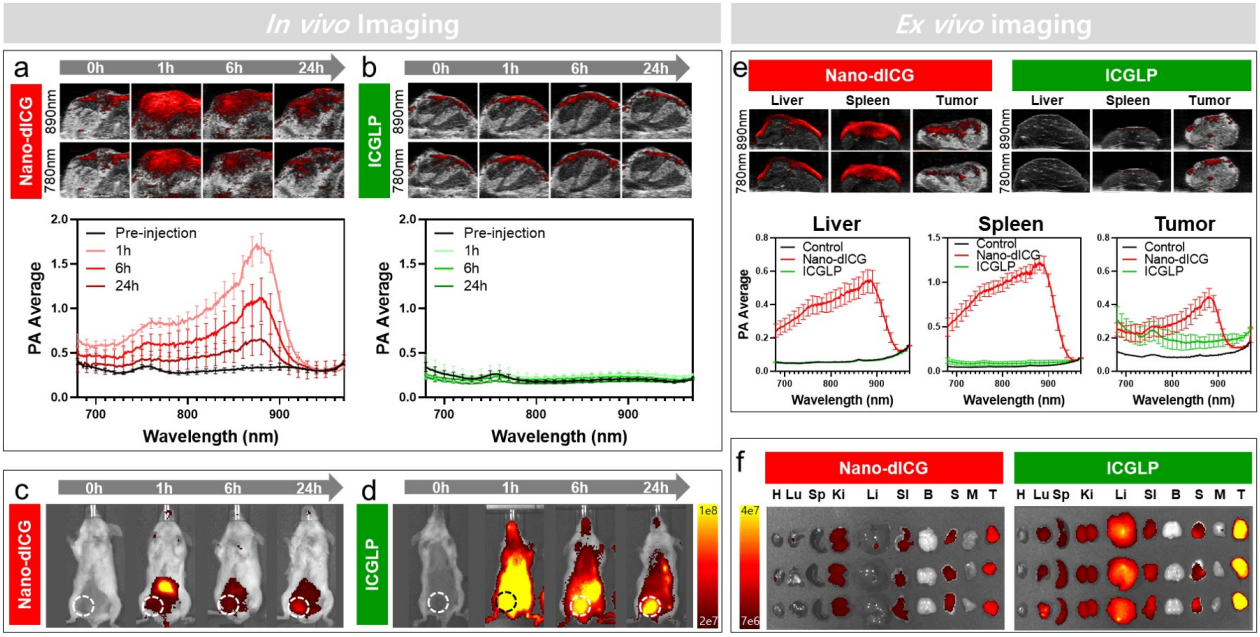

Figure 6. The PA and fluorescence imaging of Nano-dICG ($n=3$) and ICGLP ($n=3$) in 4T1 orthotopic breast cancer mouse model; Time-dependent PA imaging of tumor sites before and after intravenous injection of a) Nano-dICG or b) ICGLP (Data are expressed as the mean ± SD). Time-dependent whole-body fluorescence imaging before and after intravenous injection of c) Nano-dICG and d) ICGLP on 4T1 orthotopic tumor bearing mice. e) PA images and PA signal spectrum of excised liver, spleen and tumor at 24 h after intravenous injection of nanoparticles (Data are expressed as the mean ± SD). f) Ex vivo fluorescence images of excised organs and tumor of mice at 24 h post-intravenous injection of nanoparticles.

imaging (Figure 6c and d, Figure S18 ($n=3$)). Given that ICGLP exhibited a strong PA signal at 780 nm in the phantom test (Figure 5c and d), it was surprising to see no PA signal in the living tumors of the ICGLP group. This may suggest that ICGLP is less stable in the in vivo environment, resulting in the release of free ICG and loss of PA imaging capability. These results underscored that Nano-dICG-enabled in vivo PA imaging was attributed not only to its spectral-distinct PA signal but also its superb stability. At 24 h post-injection, the mice were sacrificed and major organs of interest including tumor, liver, and spleen were harvested for ex vivo PA imaging. As shown in Figure 6e and Figure S19, the Nano-dICG group exhibited a strong 890 nm PA signal in the liver, spleen, and tumor, indicating that Nano-dICG accumulated in the major organs where nanoparticles are usually delivered, and remained mostly in the J-aggregate intact form. In contrast, a negligible PA signal was observed in the liver, spleen and tumor of the ICPLP group (Figure 6e), while strong fluorescence was observed in those organs (Figure 6f and S18 ($n=3$)). It is expected that the organs of Nano-dICG group exhibited much lower fluorescence signal than those of the ICGLP group (Figure 6f and S20 ($n=3$)) because the dICG building block ensured a high fluorescence quenching rate for both intact (>98 %) and disrupted (>90 %) Nano-dICG (Figure 1b). Importantly, we detected a pure dICG counterpart in the tissues (liver, spleen and tumor) of the Nano-dICG group via UPLC analysis, confirming the structural stability of dICG in biological environment (Figure S21).

For the Nano-dICG-administrated mice, spleen and liver showed 3,4-fold higher PA signal than the tumor, which was consistent with their determined dICG amount by UPLC. However, the fluorescence signal in these organs was much lower than that observed in the tumor, which might suggest that Nano-dICG delivered into liver and spleen mostly retains in a J-aggregated dICG form. The metabolism of Nano-dICG in various organs remains a direction of future study. Overall, the ultra-stable phototheranostic properties, together with remarkable structural stability in the in vivo environment, in which Nano-dICG persisted in its J-aggregate dICG phase traversing various organs, make Nano-dICG a powerful in vivo NIR PA imaging agent.

Nano-dICG Permitted Potent Photothermal Therapy Efficacy

Given the improved PCE and superb photostability, paired with their unprecedented structure stability in vivo, we hypothesized that Nano-dICG would be a highly potent photothermal agent. We next evaluated its PTT efficacy in the orthotopic 4T1 breast cancer mouse model compared to ICG and ICGLP. Briefly, when the tumor volume reached approximately 100 mm^3, Nano-dICG, ICG or ICGLP (7.7 $mg\,kg^{-1}$) were intravenously injected into each group of mice. After a desired drug-light interval (DLI), the mice received 190 $J\,cm^{-2}$ light irradiation on their tumor site using an 825 nm laser and a thermal imaging camera was used to record the real-time temperature rise of the tumors during laser irradiation. As illustrated in Figure 7a, we selected a

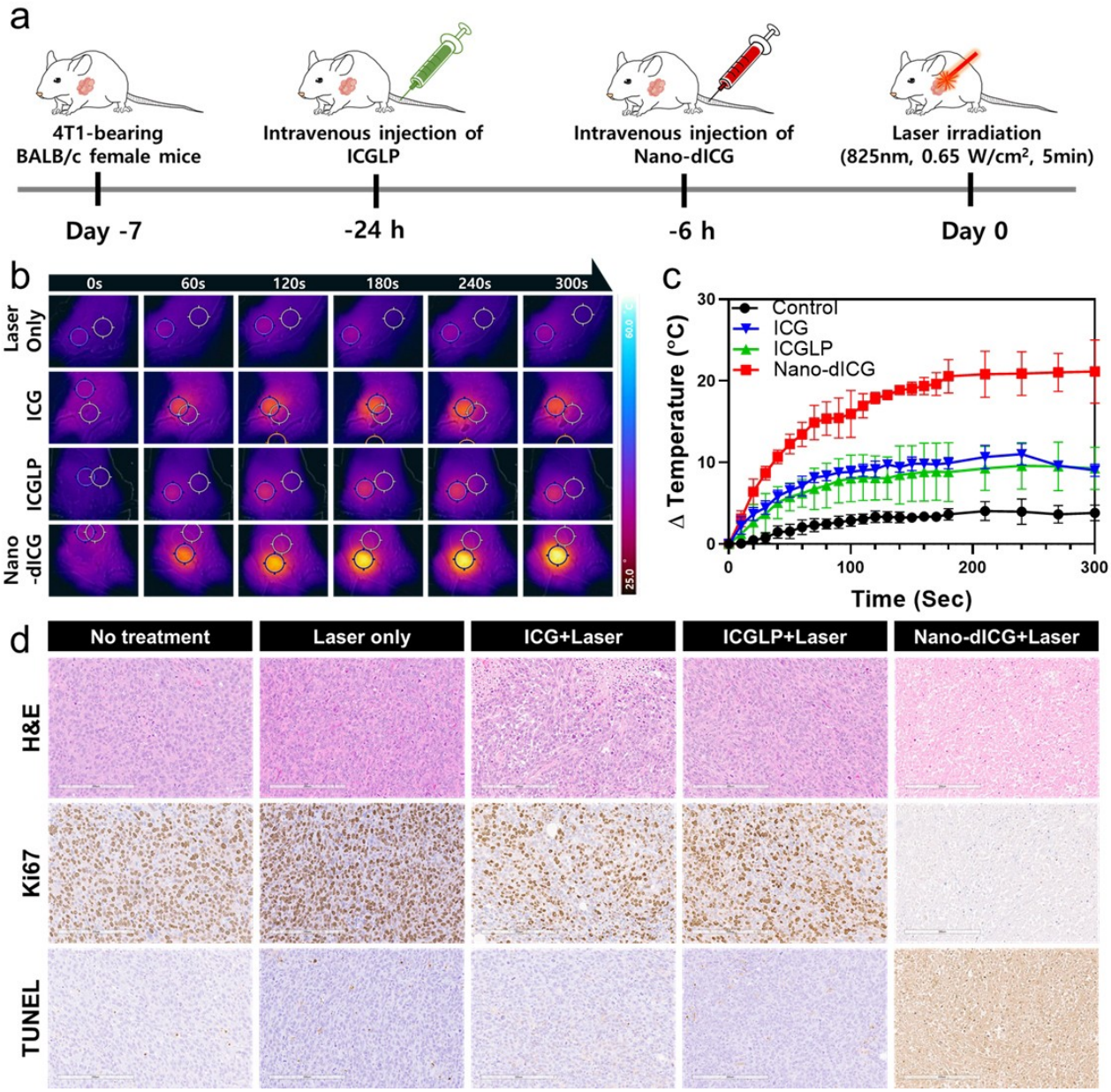

Figure 7. In vivo PTT study; a) experimental flow chart for Nano-dICG and ICGLP based PTT treatment on a 4T1 orthotopic tumor model with intravenous injection. b) IR thermal camera captured real-time thermal image during PTT and c) the mean temperature increases of the tumor sites were recorded by IR thermal camera under 825 nm laser irradiation (0.65 W cm^{-2}, $n=3$ for each group, data are expressed as the mean ± SD). d) Representative H&E, Ki67 and TUNEL stained sections of tumors of different groups at 24 h post treatment of each group (scale bar = 200 μm).

DLI of 6 h for the Nano-dICG group based on the in vivo PA imaging data (Figure 6a), which confirmed a strong tumor PA signal at 6 h post administration. The ICG group was treated at the same DLI for comparison. As the PEGylated liposomal particles usually have a longer circulation half-time of over 16 h,[23] a 24 h of DLI was used for ICPLP-PTT. Upon light irradiation (Figure 7b and c), the control group without receiving the drugs showed minimal tumor temperature increase (≈4 °C). The tumors of ICG and ICGLP groups showed a tumor temperature increase of about 10 °C, while Nano-dICG group enabled a significant temperature increase of >22 °C, and the high tumor temperature remained constant for 5 minutes during laser irradiation (Figure 7c). This demonstrates that Nano-dICG, with improved PCE and enhanced photostability, led to significantly enhanced PTT efficacy. After light treatment, one cohort of mice was sacrificed, and their tumor tissues were collected and analyzed for histopathological changes using H&E, Ki67 and TUNEL staining. As shown in Figure 7d, compared with no treatment control, tumors from laser control, ICG-PTT and ICGLP-PTT groups ($n=3$ per group) demonstrated minimal PTT response with no observable

changes in H&E- and Ki67-stained sections and no significant apoptosis confirmed by TUNEL assay.[24] In contrast, the Nano-dICG-PTT group exhibited significant evidence of tumor tissue damage, a decrease in Ki67 proliferation staining[25] and significant apoptosis staining confirmed by the TUNEL assay. In addition, no obvious cellular damage and morphology change were observed in the healthy organs of Nano-dICG groups compared to no treatment control (Figure S22), indicating that the Nano-dICG-PTT is a safe treatment approach.

A long-term survival study of Nano-dICG-PTT was then assessed on a separate cohort of mice with five groups, including no-treatment control, a laser only control, a Nano-dICG only control, a Nano-dICG-PTT group, and an ICGLP-PTT group ($n=5$ per group). The laser treatment groups received the same PTT dose following the flow shown in Figure 7a. The size of the tumors was monitored prior to treatment and every 2–3 days after treatment for 16 days until tumor size reached to the endpoint of 1000 mm^3. Noticeably, scarring was observed on the tumors in Nano-dICG-PTT group at 2 days post PTT (Figure S23), indicating its potent PTT efficacy. The scarred areas gradually healed over time, while the other groups, including ICGLP-PTT group did not show any tissue ablation (see Figure S24–S27). As a result, compared to the rapid tumor growth of the no-treatment control, the laser-only control, ICGLP + laser, or Nano-dICG-only group showed minimal tumor inhibition effects (Figure 8a). In contrast, the Nano-dICG-PTT demonstrated significant tumor growth suppression ($P \leq 0.0001$). The Nano-dICG-PTT treated mice enabled a 100 % survival rate compared to 0 % survival for all other groups at 16 days post-treatment ($P \leq 0.05$) (Figure 8b). Mice from all treatment groups demonstrated no abnormalities, such as weight loss (Figure S28). Therefore, the Nano-dICG strategy demonstrated a highly potency in PTT while maintaining safety, providing a promising solution to overcome the limitations of ICG and facilitate its clinical application in PA imaging-guided PTT.

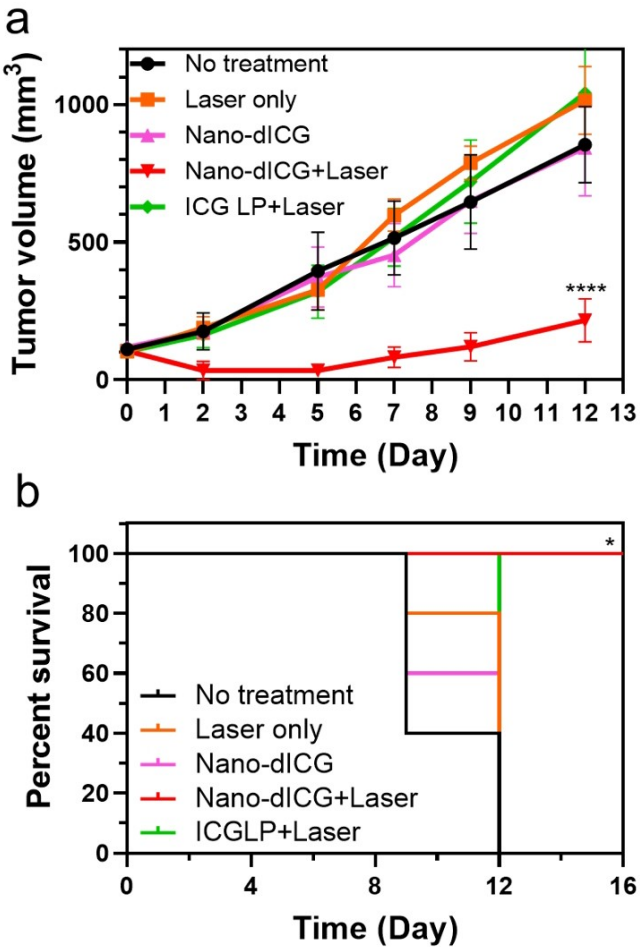

Figure 8. A long-term survival study of mice with five groups ($n=5$/group); a) Tumor growth curves were plotted by continually monitoring tumor size every day after treatment until tumor size reached the endpoint (mean ± SD, significance was determined using two-way ANOVA, wherein all groups were compared to the Nano-dICG + Laser group (**** $P \leq 0.0001$), and b) corresponding survival curves for each group. Nano-dICG + Laser group showed a significant difference (* $P \leq 0.05$).

Conclusion

Our research revealed that the stabilization of nanoemulsion with ICG facilitated ICG molecular oxidative dimerization and J-aggregation spontaneously at the interface, resulting in production of Nano-dICG composed of J-aggregated dimeric ICG counterpart. The characterization of this Nano-dICG demonstrated that dICG underwent a significant fluorescence quenching and improvements in photostability and PCE compared to ICG, leading to its potential photothermal application to overcome the limited photostability of ICG. The J-aggregation of Nano-dICG enabled intense absorption at 890 nm, together with its remarkable structural stability in vivo, giving Nano-dICG a desirable PA contrast agent for real-time tracking drug delivery at the NIR wavelength of 890 nm, which is spectral-distinct from the natural endogenous signal. Guided with its PA imaging, Nano-dICG-PTT demonstrated superior therapeutic efficacy over other ICG groups on 4T1 orthotopic tumor mouse model and significantly prolonged the survival of animals. To the best of our knowledge, this study is the first to disclose dICG as a promising photothermal conversion material. Overall, our unprecedented finding of nanostructure-driven ICG-dimerization leads to an ultra-stable phototheranostics nanoplatform, potentializing ICG's clinical application in photoacoustic imaging-guided PTT.

Acknowledgements

The study was supported by the Princess Margaret Cancer Foundation; Terry Fox New Frontiers Program Project Grant (#1075); Canadian Institute for Health Research (FDN154326); Canada Foundation for Innovation (NIF21765); Canada Research Chairs Program (950-232468); FAPESP (Fundação de Amparo à Pesquisa do Estado de São Paulo) grants: CEPOF 2013/07276-1, INCT

2014/50857-8, and scholarship HHB 2016/14033-6; CNPQ (Conselho Nacional de Desenvolvimento Científico e Tecnológico) grants: INCT 465360/2014-9; CNPq-PQ 305176/2021-8 and 140537/2022-8; CAPES (Coordenação de Aperfeiçoamento de Pessoal de Nível Superior) scholarships of GOJ 88887.495902/2020-0, LPM 88887. 513082/2020-00 and VGF 88887.636097/2021-00.Conflict of Interest

The authors declare no conflict of interest.

Data Availability Statement

The data that support the findings of this study are available from the corresponding author upon reasonable request.

Keywords: Indocyanine Green · Nanoemulsion · Photoacoustic Imaging · Photostability · Photothermal Therapy

[1] a) Y. Wen, C. L. Schreiber, B. D. Smith, *Bioconjugate Chem.* **2020**, *31*, 474–482; b) Y. Liu, P. Bhattarai, Z. Dai, X. Chen, *Chem. Soc. Rev.* **2019**, *48*, 2053–2108; c) L. Zhao, X. Zhang, X. Wang, X. Guan, W. Zhang, J. Ma, *J. Nanobiotechnol.* **2021**, *19*, 335; d) Y. Hou, X. Yang, R. Liu, D. Zhao, C. Guo, A. Zhu, M. Wen, Z. Liu, G. Qu, H. Meng, *Int. J. Nanomed.* **2020**, *15*, 6827–6838; e) C. S. Jin, J. F. Lovell, J. Chen, G. Zheng, *ACS Nano* **2013**, *7*, 2541–2550; f) X. Deng, Z. Shao, Y. Zhao, *Adv. Sci.* **2021**, *8*, 2002504; g) Q. Chen, L. Xu, C. Liang, C. Wang, R. Peng, Z. Liu, *Nat. Commun.* **2016**, *7*, 13193.

[2] a) S. Mallidi, S. Anbil, A.-L. Bulin, G. Obaid, M. Ichikawa, T. Hasan, *Theranostics* **2016**, *6*, 2458–2487; b) R. Jiang, J. Dai, X. Dong, Q. Wang, Z. Meng, J. Guo, Y. Yu, S. Wang, F. Xia, Z. Zhao, X. Lou, B. Z. Tang, *Adv. Mater.* **2021**, *33*, 2101158.

[3] a) C. Liu, S. Zhang, J. Li, J. Wei, K. Müllen, M. Yin, *Angew. Chem. Int. Ed.* **2019**, *58*, 1638–1642; b) M. Su, Q. Han, X. Yan, Y. Liu, P. Luo, W. Zhai, Q. Zhang, L. Li, C. Li, *ACS Nano* **2021**, *15*, 5032–5042; c) N. Amreddy, A. Babu, R. Muralidharan, J. Panneerselvam, A. Srivastava, R. Ahmed, M. Mehta, A. Munshi, R. Ramesh, *Adv. Cancer Res.* **2018**, *137*, 115–170.

[4] a) Z. Sheng, D. Hu, M. Xue, M. He, P. Gong, L. Cai, *Nano-Micro Lett.* **2013**, *5*, 145–150; b) R. W. Flower, B. F. Hochheimer, *Johns Hopkins Med. J.* **1976**, *138*, 33–42; c) H. Shinohara, A. Tanaka, T. Kitai, N. Yanabu, T. Inomoto, S. Satoh, E. Hatano, Y. Yamaoka, K. Hirao, *Hepatology* **1996**, *23*, 137–144; d) O. Reuthebuch, A. Häussler, M. Genoni, R. Tavakoli, D. Odavic, A. Kadner, M. Turina, *Chest* **2004**, *125*, 418–424; e) R. Liu, J. Tang, Y. Xu, Y. Zhou, Z. Dai, *Nanotheranostics* **2017**, *1*, 430–439.

[5] J. T. Alander, I. Kaartinen, A. Laakso, T. Pätilä, T. Spillmann, V. V. Tuchin, M. Venermo, P. Välisuo, *Int. J. Biomed. Imaging* **2012**, *7*, 0.

[6] V. Saxena, M. Sadoqi, J. Shao, *J. Pharm. Sci.* **2003**, *92*, 2090–2097.

[7] A.-K. Kirchherr, A. Briel, K. Mäder, *Mol. Pharmaceutics* **2009**, *6*, 480–491.

[8] a) C. Shirata, J. Kaneko, Y. Inagaki, T. Kokudo, M. Sato, S. Kiritani, N. Akamatsu, J. Arita, Y. Sakamoto, K. Hasegawa, N. Kokudo, *Sci. Rep.* **2017**, *7*, 13958; b) F. Di Nezza, G. Guerra, C. Costagliola, L. Zeppa, L. Ambrosone, *Dyes Pigm.* **2016**, *134*, 342–347.

[9] a) H. Wang, X. Li, B. W.-C. Tse, H. Yang, C. A. Thorling, Y. Liu, M. Touraud, J. B. Chouane, X. Liu, M. S. Roberts, X. Liang, *Theranostics* **2018**, *8*, 1227–1242; b) M. Sevieri, F. Silva, A. Bonizzi, L. Sitia, M. Truffi, S. Mazzucchelli, F. Corsi, *Front. Chem.* **2020**, *8*, 535.

[10] a) P. Zhao, M. Zheng, C. Yue, Z. Luo, P. Gong, G. Gao, Z. Sheng, C. Zheng, L. Cai, *Biomaterials* **2014**, *35*, 6037–6046; b) B. Qi, A. J. Crawford, N. E. Wojtynek, M. B. Holmes, J. J. Souchek, G. Almeida-Porada, Q. P. Ly, S. M. Cohen, M. A. Hollingsworth, A. M. Mohs, *Nanomed. Nanotechnol. Biol. Med.* **2018**, *14*, 769–780; c) Z. Li, Q. Yin, B. Chen, Z. Wang, Y. Yan, T. Qi, W. Chen, Q. Zhang, Y. Wang, *Nanomed. Nanotechnol. Biol. Med.* **2019**, *17*, 287–296; d) L. Zhu, P. Li, D. Gao, J. Liu, Y. Liu, C. Sun, M. Xu, X. Chen, Z. Sheng, R. Wang, Z. Yuan, L. Cai, Y. Ma, Q. Zhao, *Chem. Commun.* **2019**, *55*, 6209–6212.

[11] a) S. Shibata, N. Shinozaki, A. Suganami, S. Ikegami, Y. Kinoshita, R. Hasegawa, H. Kentaro, Y. Okamoto, I. Aoki, Y. Tamura, Y. Iwadate, *Oncotarget* **2019**, *10*, 175; b) Y. Sheng, Z. Wang, G. M. N. Neubi, H. Cheng, C. Zhang, H. Zhang, R. Wang, J. Zhou, Y. Ding, *Biomater. Sci.* **2019**, *7*, 3425–3437; c) J. C. Kraft, R. J. Y. Ho, *Biochemistry* **2014**, *53*, 1275–1283; d) R. Bhavane, Z. Starosolski, I. Stupin, K. B. Ghaghada, A. Annapragada, *Sci. Rep.* **2018**, *8*, 14455.

[12] A. Hannah, G. Luke, K. Wilson, K. Homan, S. Emelianov, *ACS Nano* **2014**, *8*, 250–259.

[13] a) M. Hutteman, J. S. D. Mieog, J. R. van der Vorst, G. J. Liefers, H. Putter, C. W. G. M. Löwik, J. V. Frangioni, C. J. H. van de Velde, A. L. Vahrmeijer, *Breast Cancer Res. Treat.* **2011**, *127*, 163–170; b) Z. Sheng, D. Hu, M. Zheng, P. Zhao, H. Liu, D. Gao, P. Gong, G. Gao, P. Zhang, Y. Ma, L. Cai, *ACS Nano* **2014**, *8*, 12310–12322.

[14] M. Tsuchimochi, K. Hayama, M. Toyama, I. Sasagawa, N. Tsubokawa, *EJNMMI Res.* **2013**, *3*, 33.

[15] F. Rüttger, S. Mindt, C. Golz, M. Alcarazo, M. John, *Eur. J. Org. Chem.* **2019**, 4791–4796.

[16] D.-H. Li, B. D. Smith, *Chem. Eur. J.* **2021**, *27*, 14535–14542.

[17] F. Würthner, T. E. Kaiser, C. R. Saha-Möller, *Angew. Chem. Int. Ed.* **2011**, *50*, 3376–3410.

[18] J. L. Bricks, Y. L. Slominskii, I. D. Panas, A. P. Demchenko, *Methods Appl. Fluoresc.* **2017**, *5*, 012001.

[19] G. Feng, G.-Q. Zhang, D. Ding, *Chem. Soc. Rev.* **2020**, *49*, 8179–8234.

[20] A. M. Goldfain, P. Lemaillet, D. W. Allen, K. A. Briggman, J. Hwang, *J. Board Agric.* **2021**, *27*, 074706.

[21] a) C. Moore, J. V. Jokerst, *Theranostics* **2019**, *9*, 1550–1571; b) A. B. E. Attia, G. Balasundaram, M. Moothanchery, U. S. Dinish, R. Bi, V. Ntziachristos, M. Olivo, *Photoacoustics* **2019**, *16*, 100144.

[22] a) L. V. Wang, J. Yao, *Nat. Methods* **2016**, *13*, 627–638; b) P. Beard, *Interface Focus* **2011**, *1*, 602–631; c) M. Xu, L. V. Wang, *Rev. Sci. Instrum.* **2006**, *77*, 041101; d) J. Weber, P. C. Beard, S. E. Bohndiek, *Nat. Methods* **2016**, *13*, 639–650.

[23] N. Beziere, N. Lozano, A. Nunes, J. Salichs, D. Queiros, K. Kostarelos, V. Ntziachristos, *Biomaterials* **2015**, *37*, 415–424.

[24] B. G. Kraupp, B. Ruttkay-Nedecky, H. Koudelka, K. Bukowska, W. Bursch, R. Schulte-Hermann, *Hepatology* **1995**, *21*, 1465–1468.

[25] W. Li, J. Yang, L. Luo, M. Jiang, B. Qin, H. Yin, C. Zhu, X. Yuan, J. Zhang, Z. Luo, Y. Du, Q. Li, Y. Lou, Y. Qiu, J. You, *Nat. Commun.* **2019**, *10*, 3349.

Manuscript received: April 20, 2023
Accepted manuscript online: May 10, 2023
Version of record online: May 31, 2023